

Orientation relationships and interfaces in directionally solidified eutectics for solid oxide fuel cell anodes

S. Serrano-Zabaleta,^a M. A. Laguna-Bercero,^a L. Ortega-San-Martín^{a,b} and A. Larrea^{a*}

^a Instituto de Ciencia de Materiales de Aragón, C.S.I.C.-Universidad de Zaragoza.

C/ María de Luna 3, E-50.018 Zaragoza, Spain.

^b Dpto. Ciencias. Sección Químicas, Pontificia Universidad Católica del Perú (PUCP).

Av. Universitaria 1801. Lima-32, Perú.

Abstract

Orientation relationships (OR), interface planes and growth directions of the directionally solidified eutectics NiO-YSZ, CoO-YSZ, NiO-CeO₂, NiO-GDC, CoO-CeO₂ and CoO-GDC have been determined by means of Electron Backscatter Diffraction (EBSD). The eutectics were prepared by the Laser Floating Zone technique at different growth rates (10-200 mm/h) to explore dissimilar lamellar spacing. The majority OR is characterized by a single $(111)_{\text{NiO/CoO}} // (001)_{\text{YSZ/GDC/CeO}_2}$ interface plane and two different growth directions: $[0\bar{1}1]_{\text{NiO/CoO}} // [010]_{\text{YSZ/GDC/CeO}_2}$ and $[\bar{1}10]_{\text{NiO/CoO}} // [110]_{\text{YSZ/GDC/CeO}_2}$, the OR being the same for both cases. In addition, a cube-on-cube OR, where the crystallographic axes of the component phases are parallel, has also been observed. These experimental results are discussed in terms of the ionic charge balance and the lattice misfit at the interface. The coincidence of reciprocal lattice points model (CRLP) has also been applied to the NiO-YSZ case. The most favourable ORs predicted by the CRLP model are consistent with the experimental findings.

Keywords: EBSD, CRLP, SOFC, DSE, Orientation imaging microscopy

**Corresponding author:*

Angel Larrea

Instituto de Ciencia de Materiales de Aragón, CSIC-Universidad de Zaragoza.

C/ María de Luna 3, E-50.018 Zaragoza, Spain

Tel.: +34 876 555125 Fax: +34 976761957 e-mail: alarrea@unizar.es

1. Introduction

1 In recent decades, solid oxide fuel cells (SOFCs) have been deemed a clean alternative to
2
3
4 convert chemical energy into electricity with high efficiency.^{1,2} One of their most notable features
5
6 is their ability to use a wide variety of fuels, which positioned them to be used in the current
7
8 distribution network of natural gas and liquid fuels. The state-of-the-art SOFC materials are: a
9
10 mixed conducting oxide as cathode, a YSZ (yttria-stabilized-zirconia) electrolyte and a porous
11
12 cermet of Ni and YSZ as anode.³ The anode has to provide electronic and ionic conductivity as
13
14 well as permeation of the fuel gas. The electrochemical reactions take place at the Triple Phase
15
16 Boundary (TPB) where metal, ionic conductor and pores meet, and thus, the TPB length should
17
18 be as high as possible. These anodes have traditionally been fabricated by sintering a mixture of
19
20 NiO and YSZ powders that subsequently undergoes reduction forming a porous ceramic-metal
21
22 composite. There are still some unresolved issues regarding the anode performance, such as the
23
24 low stability against redox cycling⁴ and the coalescence of the metal particles during cell
25
26 operation as a result of the low wettability with the ceramic phase.⁵ This coarsening results in the
27
28 degradation of the anode performance due to the loss of electronic conductivity, the obstruction
29
30 of the pores and a less efficient catalysis.
31
32
33
34
35
36
37

38 Some other materials, such as cermets of Ni and gadolinium-doped ceria (GDC), have been
39
40 proposed for SOFC anodes, mainly when GDC is used as an electrolyte. As GDC activation
41
42 energy is lower than that of YSZ, SOFC using this type of electrolyte could work at lower
43
44 temperatures, which, in return, would reduce costs of other cell components. Moreover CeO₂-
45
46 based anodes present higher resistance against redox cycling and better performance with
47
48 hydrocarbon fuels^{6,7} On the other hand, Co-based cermets such as Co-YSZ and Co-GDC have
49
50 also been proposed for SOFC. Cobalt is more costly than nickel, but it is a better catalyzer and its
51
52 sulphur tolerance is higher.^{8,9}
53
54
55
56
57
58
59
60
61
62
63
64
65

1 The properties of the anode materials are highly dependent on the microstructure and on the
2 metal-ceramic interface.^{10,11,12} In general, when using conventional preparation methods, it is not
3 possible to exert control on the metal-ceramic interfaces. Alternatively, a porous cermet obtained
4 through reduction of a directionally solidified eutectic (DSE) of NiO-YSZ, CoO-YSZ or CoO-
5 GDC has been proposed for anode.¹³ Using this method it is possible to prepare aligned
6 composite structures that, after reduction of the transition metal oxide, will result in a porous
7 cermet. In a eutectic process the liquid solidifies simultaneously into two or more solid phases,
8 producing a fine and homogeneous microstructure. In general DSE oxides present good
9 mechanical properties in comparison with conventional ceramics, as well as better stability at
10 high temperature operation.¹⁴ Eutectic growth is ruled by minimization of the interfacial energy,
11 which, for the compositions studied in this paper, results in the formation of a self-organized
12 lamellar microstructure with low-energy interfaces. The constituent phases are well aligned along
13 the solidification axis and the phase size can be tailored by choosing the solidification rate
14 according to the Hunt-Jackson law.¹⁵ The channeled microstructure of these cermets allows easy
15 gas flow and electronic conduction through the metallic porous lamellae, whereas the ceramic
16 scaffold provides an appropriate coefficient of thermal expansion (CTE) to get good
17 thermomechanical integration with the electrolyte.^{16,17} Moreover, the interfaces in this type of
18 cermets are different to those found in conventional Ni-YSZ anodes, which give rise to improved
19 anode properties and, specifically, better resistance against ageing.^{18,19} For a good understanding
20 of the metal-ceramic interfaces formed after reduction of the eutectic composite, prior
21 understanding of both the oxide-oxide interfaces formed in the eutectic and of the parameters
22 controlling its formation is essential.^{20,21,22} This being the main objective of the paper.

23
24
25
26
27
28
29
30
31
32
33
34
35
36
37
38
39
40
41
42
43
44
45
46
47
48
49
50
51
52
53 Minford *et al.*²³ established in 1979 the two main factors that determine the interface plane and
54 the orientation relationship in directionally solidified eutectics: the balance of charge at the
55 interface and the minimization of the lattice misfit. Several models have been developed in order
56 to predict or account for experimental orientation relationship between phases and interphase
57
58
59
60
61
62
63
64
65

1 configuration in different systems, based upon atomistic considerations (such as Density
2 Functional Theory),^{24,25} or geometrical considerations in 2D (Near Coincidence Site Lattice,
3 NCSL)^{26,27} or 3D (Coincidence of Reciprocal Lattice Points, CRLP).²⁸ The latter is based upon
4 the hypothesis that most stable configurations correspond to relative orientations where the
5 crystal lattices at the interphase suffer the minimum possible distortion in terms of interplanar
6 spacing continuity. The CRLP model was developed to study heterophase interfaces and it has
7 proved able to account for orientation relationships between phases in metal/ α -Al₂O₃ systems,²⁹
8 as well as in Ni films deposited on YSZ by the pulsed laser deposition technique.³⁰

9
10
11
12
13
14
15
16
17
18
19 In this paper, using Electron Backscattering Diffraction (EBSD), we have characterized the
20 growth direction, interface plane and orientation relationship between the component phases of a
21 family of eutectics. In recent years the EBSD technique has become a powerful microstructural
22 characterization tool which is highly appropriate for studying relatively large surface samples
23 displaying one or more orientation relationships.³¹ The eutectics studied are formed by a
24 transition metal oxide (NiO or CoO) and an ionic conductor (YSZ and GDC) that can be used as
25 precursors for SOFC anodes. NiO-CeO₂ and CoO-CeO₂ have also been included in the paper for
26 comparison with the doped ceria eutectics. The experimental results are discussed in terms of the
27 balance of charge density at the interface and of the lattice misfit. To determine the orientation
28 relationship that correspond to the optimum geometrical coherence between the constituent
29 phases, the CRLP model has been applied.

46 47 **2. Experimental details**

48 49 *2.1 Preparation of the samples*

50
51
52
53 Directionally solidified eutectic materials combining NiO or CoO, as precursor of the
54 transition metal component of the cermet (TMO=NiO, CoO), and YSZ, GDC or CeO₂ as ionic
55 conductors (IC=YSZ, GDC, CeO₂) were prepared using the Laser Floating Zone method (LFZ).
56 For this purpose, powders of NiO (99%, Alfa Aesar), Co₃O₄ (99.7%, Alfa Aesar), YSZ (8 mol%

1 Y₂O₃ stabilized ZrO₂, 99.9%, Tosoh), GDC obtained from inorganic salt precursors following
2 Pechini method³² and CeO₂ (99.9%, Aldrich) were mixed, isostatically pressed under 200 MPa
3 for 5 min and sintered at 1400 °C to obtain ceramic cylinders, 8 cm long and 2.5 mm in diameter.
4 Then, these ceramic precursors underwent melting and subsequent solidification using the LFZ
5 technique to obtain DSE rods with the compositions^{16,33,34,35} and solidification rates indicated in
6 Table 1. The laser used was a CO₂ continuous wave laser ($\lambda = 10.6 \mu\text{m}$; Blade600, Electronic
7 Engineering, Firenze) and the eutectics were processed in two steps. In the first step, at 200 mm/h
8 upwards, the ceramic precursor cylinder densifies and stretches, whereas the final step was
9 performed downwards at the selected growth rate. The final diameter of the eutectic rod was 2
10 mm. The CoO eutectics were grown under inert atmosphere, assuring the reduction of Co₃O₄ to
11 CoO during the first processing step. X-ray analysis proved that the cobalt oxide in the resulting
12 material was CoO.
13
14
15
16
17
18
19
20
21
22
23
24
25
26
27

28 *2.2 Electron Backscattering Diffraction experiments*

29 **Scanning Electron Microscopy** (SEM) analysis and EBSD experiments were carried out in
30 polished transverse and longitudinal cross-sections using a Merlin Field Emission SEM (Carl
31 Zeiss, Germany), with an integrated EBSD system (HKL model from Oxford Instruments, United
32 Kingdom).
33
34
35
36
37
38
39
40
41

42 The EBSD experiments were performed positioning the 70°-tilted sample at 14.5 mm from the
43 pole piece and using 20 kV of accelerating voltage and 0.8 nA of probe current. The EBSD
44 detector (model HKL EBSD system, Oxford Instruments) consists of a CCD camera that was set
45 to 514 x 384 resolution using 4x4 binning. Each Kikuchi pattern was acquired twice (60 ms of
46 acquisition time) and averaged out. The Channel5 software³⁶ was used to automatically detect 7
47 Kikuchi bands and index each pattern to determine the crystallographic orientation of the sample
48 at that very spatial point and produce an orientation map for every experiment. This software also
49 generates pole figures and calculates the lattice correlation boundary between phases. Typical
50
51
52
53
54
55
56
57
58
59
60
61
62
63
64
65

1 acquisition time of a map of a zone of about 50 x 9 μm was about 2 hours, using 0.08 μm size
2 pixels. Depending on the interphase spacing of each sample the pixel size ranged from 0.05 to 0.3
3 μm. Despite the relatively low number of bands used and the low camera resolution, it was
4 possible to determine the spatial orientation with an angular accuracy better than 0.5° due to the
5 high symmetry of the crystallographic phases involved. NiO and CoO are rock-salt structures
6 whereas YSZ, GDC and CeO₂ are fluorite structures, all of them belonging to the $Fm\bar{3}m$ space
7 group.

8
9
10
11
12
13
14
15
16
17 Specimen preparation for EBSD was performed using a progressive lapping and polishing
18 method to eliminate in each step the strains created during the previous one, which would blur the
19 Kikuchi bands that form the EBSD patterns, also known as Kikuchi patterns. Special care has
20 been taken to ensure that the sample surface is free of damage, because the EBSD patterns are
21 generated from a very thin surface layer of about 40 nm.³¹ Slices of the fibers were severed with a
22 diamond saw, and then the cross-sections were ground in successive steps with SiC (15 μm and
23 10 μm of particle size using a polishing wheel rotating at 40 rpm), polished with diamond paste
24 (3 μm and 1 μm of particle size, 120 rpm) and finally colloidal silica (0.04 μm of particle size,
25 100 rpm) for 15 min. Throughout the preparation process, the specimen was subjected to a 2.5 N
26 load. Since colloidal silica might cause differential polishing between the phases, the duration of
27 this treatment was chosen with the aim of obtaining a conveniently polished surface with only
28 slight differential polishing. Differential polishing had to be kept to a minimum to avoid shadows
29 in the orientation maps due to the tilted position of the sample. This shadowing effect is
30 particularly important for eutectics grown at high rates because they display low interlamellar
31 spacing.

32 33 34 35 36 37 38 39 40 41 42 43 44 45 46 47 48 49 50 51 52 53 54 55 56 57 58 59 60 61 62 63 64 65 *2.3. Coincidence of Reciprocal Lattice Points (CRLP) calculation procedure*

In order to determine the most favorable orientation relationship between the component phases of the eutectic we have used the CRLP method.²⁸ In order to apply this method we have

developed a Matlab code that calculates the overlapping of the reciprocal lattices of two phases of the eutectic. Each point P of the reciprocal lattice is associated with a family of the real lattice planes (hkl) as follows: $OP_{hkl}=h\cdot a^*+k\cdot b^*+l\cdot c^*$, where a^* , b^* and c^* are the primitive vectors of the reciprocal lattice, the modulus of the OP_{hkl} vector being proportional to the inverse of the interplanar spacing.³⁷ The coincidence, or more precisely the near-coincidence of the reciprocal lattices, is calculated assuming that each point of the reciprocal lattices has spherical shape with radius r^* . We have placed small spheres at the reciprocal lattice points and superpose both lattices according to a given orientation relationship. We have then calculated the intersection volume between all of the spheres for every possible orientation relationship. Those orientation relationships that yield the highest intersection volumes are the most favorable ones according to this model, since this means that there are several family planes with similar interspacing parallel to each other, that is to say, there is little discontinuity at the interface formed for that orientation relationship.

In the work presented in this paper, we took into account all reciprocal lattice points contained in a sphere of radius $6\cdot a^*$ ($a^*=2\pi/a$), where a is the cell parameter of the TMO. The same volume considered for the IC phase included more points, since the cell parameters of the studied IC here are bigger than those of the TMO (NiO and CoO). The radius of the small spheres sited at the reciprocal lattice points was $0.2\cdot a^*$. For the calculation of the overlapped volume as a function of the OR, the TMO lattice was set fixed and the IC phase was rotated in steps of 1° using the Euler angles. We used the ZXZ' convention for the Euler angle definition and reduced the Euler space to $\alpha \in (0, 90^\circ)$, $\beta \in (0, 90^\circ)$ and $\gamma \in (0, 90^\circ)$ due to the cubic symmetry of the phases.³⁸

3. Experimental results

3.1 Microstructure

Cylinders of NiO-YSZ, CoO-YSZ, NiO-GDC, NiO-CeO₂, CoO-GDC and CoO-CeO₂ in their eutectic composition were grown following the process described above, and slices were cut

perpendicular to the solidification direction, i.e. perpendicular to the cylinder axis. Those transverse cross-sections were analyzed in a SEM. Lamellar microstructure, where NiO/CoO and YSZ/GDC/CeO₂ lamellae alternate, was found in all materials and for all solidification rates, while fibrillar microstructure was only found in the CoO eutectics solidified at low rate (10 mm/h), coexisting with the lamellar microstructure as described previously for the CoO-GDC case.²¹ In those cases, CoO fibers were embedded in a YSZ/GDC/CeO₂ matrix. The interphase spacing (λ) determined from the SEM experiments decreases with the solidification rate (v), according to Hunt-Jackson law: $v \cdot \lambda^2 = K$, where K is a constant which depends on the material and the thermal gradient for each fabrication method.¹⁵ The value of the interphase spacing obtained is indicated in Table 1.

3. 2. Orientation relationships, growth directions and interface planes

EBSD experiments were performed to determine the growth directions, interface planes and orientation relationships between phases. We analyzed the fibrillar and the lamellar areas in the central area of the transverse cross-sections as well as in peripheral zones. In these kinds of experiments, an Electron Backscattered Pattern (EBSP) is obtained from every point on the sample surface hit by the electron beam. The EBSP reflects the crystal symmetry of the point from which it has been taken as well as the spatial orientation, which can be determined from the position of the Kikuchi bands (an example of an EBSD pattern is shown in Fig. 1). In a typical orientation map, like the one shown in Fig. 2, a color or grey level is assigned to the crystallographic orientation according to a conventional scheme.³⁶³⁶ As a consequence, all the pixels displaying the same grey level have the same crystallographic orientation and form a crystallographic grain if connected to each other. In Fig. 2, it can be seen that there are orientation deviations between eutectic grains (up to 20°), but within each grain, each phase behaves as a single crystal.

3.2.1 Lamellar areas

The growth direction of each phase can be determined from the pole figures (Fig. 3). They appear as low Miller index crystal axes parallel to the cylinder axis, ergo, to the direction that is perpendicular to the sample transverse cross-section. They can be identified in the pole figures as poles close to the center of the stereogram. Thus, in the majority of areas with lamellar microstructure, experiments showed two possible combinations of growth directions (GD):

| | TMO = NiO, CoO | | IC = YSZ, GDC, CeO ₂ |
|------|----------------|--------------------|---------------------------------|
| GD1: | $[0\bar{1}1]$ | // | $[010]$ |
| GD2: | $[\bar{1}10]$ | $\sim 15^\circ //$ | $[110]$ |

where, between all the possible symmetry equivalent options, we have chosen a sign criteria that we will maintain throughout the paper. In both cases, the rock-salt structure phase (TMO = NiO, CoO) grows along the $\langle 110 \rangle$ crystal axis, while the fluorite structure phase (IC = YSZ, GDC, CeO₂) may grow along the $\langle 100 \rangle$ axis as well as along the $\langle 110 \rangle$ axis. In the former case, growth directions $[0\bar{1}1]_{\text{TMO}}$ and $[010]_{\text{IC}}$ are fully parallel (growth direction GD1). In the latter, $[\bar{1}10]_{\text{TMO}}$ and $[110]_{\text{IC}}$ are 15° misoriented (growth direction GD2).

Table 2 summarizes the growth directions found for each material studied at all solidification rates. Some authors suggested that the appearance of GD1 or GD2 could depend, among other factors, on the solidification rate.²⁰ However, the experimental results obtained in this work do not confirm this suggestion.

Interface planes were determined from the orientation maps and pole figures. The interface planes from both phases are parallel to each other and, as they are represented in the pole figure by their perpendicular axes, they can be identified as poles close to the stereogram periphery. We also verified that these planes correspond to the projection of the interface planes observed in the orientation map. Moreover, the EBSD Channel5 software³⁶ enables the calculation of the relative

1 orientation for any pair of axes or planes from the different phases, the so-called *lattice*
2 *correlation boundary component*, and represents it in the orientation map. Thus, it is possible to
3 calculate the misorientation for the given directions at every point of the interface drawn in the
4 orientation maps. Moreover, quantitative data can be inferred from the misorientation histograms.
5 This tool was used to verify the interface planes, namely, $(111)_{\text{TMO}}// (001)_{\text{IC}}$ for GD1 and GD2
6 cases. Misorientation between these planes was calculated in all experiments, and in most cases it
7 is lower than 1° , while the best angular resolution is 0.5° for this experimental setup, which
8 confirms that $(111)_{\text{TMO}}// (001)_{\text{IC}}$ are the actual interface planes.
9

10
11 In addition to the above-described OR, which is the most commonly found, we have observed
12 the presence in some areas of a cube-on-cube OR, where the crystal axes of both phases are
13 parallel. From the pole figures in this case the growth direction seems to be $[111]$ or $[110]$,
14 depending on the zone analyzed. Fig. 4 shows an orientation map acquired over a longitudinal
15 cross-section of a NiO-YSZ sample solidified at 10 mm/h where the cube-on-cube orientation
16 relationship appears. With the aim of determining the interface plane for the zones with the
17 minority OR, we performed additional EBSD experiments on transverse and longitudinal cross-
18 sections of NiO-YSZ solidified at 10 mm/h, since this was one of the materials and solidification
19 rates in which the cube-on-cube OR appears more frequently. In the orientation maps the lines we
20 observe representing the interface plane are produced by the intersection between the interface
21 plane and the sample surface, and they correspond to vectors contained in the interface plane. As
22 we can determine the crystallographic coordinates of these vectors from the orientation maps, the
23 interface plane is obtained by doing the cross product of the intersection vectors obtained from
24 transverse and longitudinal cross-sections. This procedure is not without its ambiguity, because
25 the two vectors are obtained from different specimens. However, using vectors from different
26 zones we have verified that the cross product results in a unique interface plane with coordinates
27 of about $(0.185, 0.188, 0.965)$, which forms $\sim 15^\circ$ with the (001) plane.
28
29
30
31
32
33
34
35
36
37
38
39
40
41
42
43
44
45
46
47
48
49
50
51
52
53
54
55
56
57
58
59
60
61
62
63
64
65

3.2.2 Fibrillar areas

1 In the fibrillar zones, similar results were found in the case of the CoO-GDC, where the
2 growth directions and lattice correlation boundary are the same as described for the majority
3 orientation relationship in lamellar areas (Fig 5a). Nonetheless, CoO-CeO₂ and CoO-YSZ
4 fibrillar areas showed different behavior. The orientation of the crystallographic axes varies
5 throughout the same transverse cross-section, and there is no defined growth direction (Fig 5b).
6 The orientation relationship between the phases also changes from one experiment to another.
7 Furthermore, a cube-on-cube orientation relationship was found in CoO-CeO₂ and CoO-YSZ
8 fibrillar areas, whereas it was not observed in fibrillar CoO-GDC.
9
10
11
12
13
14
15
16
17
18
19
20
21

4. Discussion

22 The particular properties of DSE materials are mostly due to their special interfaces, which are
23 clean and strong, without interfacial precipitates. The nature of these interfaces stems from the
24 thermodynamics ruling the eutectic growth, i.e., the minimization of the interfacial energy.
25 Minford *et al.* were the first authors who reviewed the characteristic of the interfaces in DSE.²³
26 They pointed out that the orientation relationships in DSE result from two main factors:
27 minimization of the lattice misfit between phases and the optimum matching between ionic
28 charge densities of the polar planes involved. The interfaces are thought to be made up of a single
29 plane of oxygen atoms, common to both crystal structures³⁹ and therefore, the non-directional
30 ionic forces within each phase bond ions beyond the interface, strongly joining the phases in the
31 DSE. These low-energy interfaces made up of polar planes may contribute to the exceptional
32 microstructural stability of the studied materials. Hitherto, only one experimental direct
33 observation of the interface being made up of a single plane of oxygen atoms has been reported: a
34 HRTEM image combined with an EELS experiment carried out by E.C. Dickey *et al.*⁴⁰ However,
35 to get these kinds of images the zone axes of both phases have to be perfectly parallel at the
36 interface, and this is not the common situation in DSE. To determine the OR between the phases
37
38
39
40
41
42
43
44
45
46
47
48
49
50
51
52
53
54
55
56
57
58
59
60
61
62
63
64
65

and the interfacial planes we used mainly EBSD because it enables us to obtain this information throughout an extensive area of the sample surface.

4.1. Growth directions, orientation relationship and interface planes

EBSD experiments showed that there are two possible growth directions: $[110]_{\text{TMO}}$ fully parallel to $[100]_{\text{IC}}$ (growth direction GD1), and $[110]_{\text{TMO}}$ and $[110]_{\text{IC}}$ 15° misoriented (growth direction GD2). The interface planes are, in both cases, $(111)_{\text{TMO}}$ and $(001)_{\text{IC}}$. These growth directions have been previously reported in samples grown at different rates and using different methods,^{20,21,41,42,43} but it should be pointed out that they do correspond to the same orientation relationship between the interface planes.

The relative orientation of the interface plane atoms between the phases is shown in Fig. 6. The geometric configuration of these planes determines that whenever the axes $[\bar{0}11]_{\text{TMO}}$ and $[010]_{\text{IC}}$ are parallel, $[\bar{1}10]_{\text{TMO}}$ and $[110]_{\text{IC}}$ appear 15° systematically misoriented. Thus, it can be inferred that the relative orientation between TMO and IC phases is unique despite the growth direction. To represent the interfacial coincidence in a clear picture is not an easy task because the ions in the TMO phase are divalent whereas the ions in IC are either divalent, trivalent or tetravalent. As it is usually assumed that the interfacial plane is made up of a common oxygen plane, which maintains the anion-cation sequence of planes, we considered it was more coherent to show the coincidence between $(001)_{\text{IC}}$ oxygen ions and $(111)_{\text{TMO}}$ transition metal ions. Another valid criterion could be to represent the coincidence of oxygen ions from both phases. As a common oxygen plane forms the interface, it would have to be in a mixed configuration between that of the component phases, with a minimum distortion. In any case, as the (111) planes of anions and cations in the TMO rock salt structures are identical, the coincidence shown in Fig. 6 is the same with either criteria.

1 The growth direction is usually identified as a crystallographic axis of the material, which is
2 oriented parallel to the solidification direction, i.e., to the cylinder axis. This axis can be
3 identified in the pole figure as a pole close to the centre of the stereogram. A pole situated exactly
4 at the centre of the pole figure is seldom found. Small deviations might be due to the
5 solidification front curvature or any other small experimental deviation. However, since the
6 interfacial planes are always $(111)_{\text{TMO}}// (001)_{\text{IC}}$, and the orientation relationship between these
7 interface planes is the same for GD1 and GD2, the material might not be growing exactly along
8 any preferred crystallographic axis, neither GD1 nor GD2. We believe that it is actually this
9 preferred orientation relationship that is governing the spatial orientation of the phases during the
10 solidification process. The fact that, in some cases, both GD1 and GD2 have been found over the
11 same surface is consistent with this idea. Moreover, the component phases of these materials have
12 relatively low entropy of melting. Their dimensionless entropy of melting usually ranges between
13 3 and 3.5.⁴⁴ The entropy of fusion criterion of Hunt and Jackson⁴⁵ was originally proposed in
14 1966 to classify eutectic morphologies. They used a nearest-neighbour broken model and
15 thermodynamic arguments to show that the type of growth depends on the dimensionless molar
16 entropy of melting $\Delta S/R$, where ΔS is the entropy of melting and R is the ideal gases constant.
17 Substances with low entropy of fusion, generally considered if $S \leq 2$, present independence of the
18 growth kinetics with respect to the crystal direction. In these materials, the growth direction is
19 mainly governed by the heat flow and not by the crystallography of the component phases.^{46,47}

20 With respect to the cube-on-cube orientation relationship, it is not easy to quantify the
21 presence of this minority OR. Crystal growth is a rather complex matter and the occurrence of
22 different growth habits from the usual one is not surprising. However, it is important to point out
23 that we have determined the presence of the cube-on-cube OR in the whole family of eutectics
24 studied, mainly in the NiO-YSZ case grown at low rates. The cube-on-cube orientation
25 relationship has previously been reported by Minford *et al.* for MgO-MgAl₂O₄, MgO-ZrO₂ and
26 MgO-CaO DSE,²³ by Larrea *et al.* for CoO-YSZ DSE¹⁹ and by Xing *et al.* for NiO-YSZ

fabricated by Pulsed Laser Deposition.⁴⁸ As we have previously mentioned, the interface plane seems to be near the (001), but this plane is not polar in the rock-salt structure of the TMO phases, which is contradictory to what has been reported about interfaces in DSE oxides.¹⁴ Moreover the apparent interface plane is not perpendicular to one of the growth directions observed, [111]. Although this OR was first reported in 1979, there is still lack of understanding.

4.2. Ionic charge balance at the interface

As mentioned before, one of the requirements for the formation of DSE interfaces is the ionic charge density balance at the interface. The maintenance of the charge balance across the interface is a requirement of Pauling's second rule of ionic structures, because the ionic bonds extending from the interface plane must be compensated for on the polar plane of the other phase.

⁴⁹ To check the fulfilment of this rule and to determine the possible pairs of planes with good balance, the ionic charge density was calculated for low Miller indices planes (see Table 3) in all materials, as well as the misfit between each possible combination of planes. It is known that there is some Ni diffusion (2 mol%) in the YSZ in the case of the NiO-YSZ eutectic, as well as some Co diffusion (5 mol%) in the YSZ in the case of the CoO-YSZ eutectic.¹⁶ In the case of the CoO-GDC and CoO-CeO₂, there is no detectable diffusion,²¹ and in the case of the NiO-GDC and NiO-CeO₂, it has not been determined. In addition to the diffusion of Ni and Co cations into the YSZ, it was assumed that the oxygen vacancies were homogeneously distributed throughout the bulk, and that the NiO and CoO were stoichiometric. In spite of these assumptions, the lowest ionic charge density misfit, between high charge density polar planes, was found for (111)_{TMO}//(001)_{IC} for all the eutectics studied, which is the actual interface plane according to the EBSD experimental results (see Table 4). If we include in these calculations the polar planes with low charge density, we could obtain lower misfits, for instance in the (221)_{GDC} and (511)_{NiO} case. However, the stability of these interfaces between low-polarity planes would necessarily be lower.

We would like to point out that the three eutectics displaying the poorer misfit present deviations with respect to the most usual growth behaviour. CoO-YSZ (13.6 % misfit) and CoO-CeO₂ (6.7 % misfit) present fibrillar areas with neither clear growth directions nor well-defined interfacial planes. However, the CoO-GDC eutectic (4.3 % misfit) that also presents fibrillar microstructures always displays the majority OR and well defined (111)_{TMO}//(001)_{IC} interface plane. In addition, in the NiO-YSZ (9.9% misfit) and CoO-YSZ eutectics we have frequently observed the presence of the cube-on-cube orientation relationship.

4.3. Lattice matching and CRLP calculations

In order to analyse the lattice matching of the component phases, the first approximation is to calculate within the interface plane, (111)_{TMO} and (001)_{IC}, the misfit of the oxygen sublattice for the close-packed direction, $[0\bar{1}1]_{TMO}//[010]_{IC}$, and its perpendicular, $[\bar{2}\bar{1}\bar{1}]_{TMO}//[100]_{IC}$. Tiller was the first author to propose that, as lattice strain energy is a major contribution to the interface energy, the interface planes with the minimum misfit would result in favoured low-energy interfaces.⁵⁰ This misfit is calculated as $\delta = 2(l_1 - l_2)/(l_1 + l_2)$, where l_1 and l_2 are the interatomic distances along the parallel crystallographic axes of the two phases contained in the interface plane. According to the model and approximations used by Frank and Van der Merwe, coherent interfaces could be expected for misfits lower than about 9%.⁵¹ The results are shown in Table 5, where it can be observed that the calculated lattice parameters misfit is quite high in at least one of the directions for all the materials in the family.

However, this approach could be considered only a first approximation to get an idea of the lattice matching. To get further insight into this matter, we have applied the CRLP model to the eutectic growth for the first time. The ionic charge balance at the interface would explain the formation of the (111)_{TMO}//(001)_{IC} interface in the whole family studied, as well as possibly indicating a potential origin of the deviations from this behaviour. However, we would like to investigate the reasons of the appearance of the well-defined majority OR and of its deviation, the

cube-on-cube OR. Considering, moreover, that in the last case we have not identified the interface plane.

The idea that a good matching between the lattices in the interface plane is one of the factors determining the orientation relationship between phases during eutectic growth may be extended to a good matching between the lattices in 3D by considering the CRLP model. This model takes into account not only atoms contained in the interface plane, but also all the low-index Miller planes from both phases. Thus, the most favourable orientation relationships between phases are those for which there are most planes with similar interspacing parallel to each other, i.e., those that give rise to a high intersection volume between the spheres located at the reciprocal lattices of both phases.

Although the CRLP model does not consider the interface plane in the calculations, it does determine the orientation relationship that maximizes the three-dimensional lattice continuity. Therefore, the favourable orientation relationship determined by the CRLP model corresponds to the state of better 3D geometrical coherence between the two adjacent crystals, which would probably correspond to the minimum elastic strain energy at the interface.²⁹ In addition, the ability of the CRLP method to predict not only the primary orientation relationship, but also secondary orientation relationships is significant.

The results of the CRLP calculations for the NiO-YSZ DSE are shown in Fig. 7. **The extension of these calculations to the other eutectic systems will be presented in a future article.**

Fig. 7(a) is a representation of the 3D Euler space where the points marked in dark correspond to those combinations of Euler angles for which the calculated overlapped volume is the highest, above a certain threshold. It is easier to understand Fig. 7(b), where the horizontal axes correspond to the first two Euler angles, α and β , and in the vertical axis we represent the overlapped volume for each pair of α and β values and $\gamma=0$. It is possible to observe two main peaks for the values $\alpha_1=45^\circ$, $\beta_1=35.3^\circ$, $\gamma_1=0^\circ$ and $\alpha_2=45^\circ$, $\beta_2=54.7^\circ$, $\gamma_2=0^\circ$, with the same height

that represent the two absolute maxima. Analysing the rotations produced by these Euler angles we obtained two symmetrically equivalent OR corresponding to the majority orientation relationship $(111)_{\text{TMO}}//(\overline{001})_{\text{IC}}$ and $[\overline{011}]_{\text{TMO}}//[010]_{\text{IC}}$. The minority cube-on-cube orientation relationship ($\alpha=0, \beta=0, \gamma=0$) may be distinguished in Fig. 7 (b) among other secondary relative maxima.

However, due to the large number of maxima that can be observed in Fig. 7 (a), a careful study of the symmetry equivalent ORs is essential. The triplet of Euler angles characterize the rotation that we have to apply to the IC phase to place it in the same orientation as the TMO phase. Due to the high symmetry of both phases we can obtain a large number of Euler triplets associated to symmetry equivalent variants of the same orientation relationship. The orientation of each phase with respect to a fixed reference system can be characterized by a rotation matrix (S_{IC} and S_{TMO}). In this way, an Euler rotation matrix $G=G(\alpha,\beta,\gamma)$ for a particular inter-phase orientation relationship is defined by:

$$S_{\text{TMO}} = G(\alpha,\beta,\gamma) \cdot S_{\text{IC}} \quad (1)$$

If we apply to each phase a rotation of its own point group (O_i and O_j for TMO and IC respectively) we obtain symmetry equivalent orientation relationships:

$$O_i \cdot S_{\text{TMO}} = G(\alpha,\beta,\gamma) \cdot O_j \cdot S_{\text{IC}} \quad (2)$$

As a consequence, for a given rotation matrix the set of symmetry equivalent matrices is given by:

$$G(\alpha',\beta',\gamma') = O_i \cdot G(\alpha,\beta,\gamma) \cdot O_j \quad \forall O_i \in R(\text{TMO}), \quad \forall O_j \in R(\text{IC}) \quad (3)$$

where R is the group formed by the rotations of the point groups of each phase. In our case the point groups of all the phases are the same, $m\overline{3}m$ and this has 24 elements. So, in the full Euler space, $\alpha \in (0, 360^\circ)$, $\beta \in (0, 180^\circ)$ and $\gamma \in (0, 360^\circ)$, we have $24 \times 24 = 576$ Euler triplets. To

1 manage this large number of symmetry equivalent points we have implemented in our Matlab
2 code an algorithm to identify all the maxima and a procedure to calculate the symmetry
3 equivalent points for each maxima. Using these tools we have finally found that all the absolute
4 maxima represented in Fig. 7(a) have the same overlapped volume and correspond to the same
5
6 maxima represented in Fig. 7(a) have the same overlapped volume and correspond to the same
7
8 orientation relationship as the experimentally found $(111)_{\text{TMO}}//(\overline{001})_{\text{IC}}$ and $[\overline{011}]_{\text{TMO}}//[\overline{010}]_{\text{IC}}$.
9
10 However, the cube-on-cube OR, corresponds to secondary maxima, which is less commonly
11
12 found.
13
14
15
16
17

18 5. Conclusions

19
20 NiO-YSZ, NiO-CeO₂, NiO-GDC, CoO-YSZ, CoO-CeO₂ and CoO-GDC directionally
21
22 solidified eutectic ceramics have been produced by the LFZ technique at rates varying from 10 to
23
24 200 mm/h. Two types of microstructure were found in this family of eutectic materials: lamellar
25
26 and fibrillar (only for CoO eutectics solidified at low rate). Two orientation relationships were
27
28 found in the lamellar areas. The most common one is given by the following parallelisms:
29
30 $(111)_{\text{TMO}}//(\overline{001})_{\text{IC}}$ and $[\overline{011}]_{\text{TMO}}//[\overline{010}]_{\text{IC}}$. Two different growth directions were found for this
31
32 orientation relationship, and both give rise to the same interface plane: $(111)_{\text{TMO}}//(\overline{001})_{\text{IC}}$. The
33
34 less common orientation relationship found in the lamellar and fibrillar areas is the so-called
35
36 cube-on-cube, where the IC phase and the TMO phase grow parallel to each other. For this
37
38 orientation, we determined that the interface plane is a crystal plane that forms about 15° with the
39
40 (001) plane.
41
42
43
44
45
46
47

48
49 The calculations of the ionic charge balance at the interface show that, from the whole family
50
51 of eutectics studied, the best possible matching is obtained for the experimentally found
52
53 $(111)_{\text{TMO}}//(\overline{001})_{\text{IC}}$ interface plane. Moreover, the eutectics that present poorer charge balance
54
55 (CoO-YSZ, NiO-YSZ and CoO-CeO₂) also present deviations from the usual growth behavior in
56
57 the fibrillar areas when growth is at low rates.
58
59
60
61
62
63
64
65

1 The CRLP model has been applied to NiO-YSZ eutectic and predicts that the most common
2 orientation relationship observed is the most favorable one, because it corresponds to the absolute
3 maximum overlapping of reciprocal lattices calculated by the model. The less common cube-on-
4 cube orientation relationship corresponds to secondary maxima predicted by the model. Further
5 calculations are in progress to apply this model to the other eutectic of the family studied in this
6 paper.
7
8
9
10
11
12
13

14 **Acknowledgements**

15 This study was funded by the Spanish Government and Feder program of the European
16 Community (projects MAT2009-14324-C02-01 and MAT2012-30763). The use of Servicio
17 General de Apoyo a la Investigación (SAI, University of Zaragoza) is additionally acknowledged.
18
19
20
21
22
23
24
25
26
27
28
29
30
31
32
33
34
35
36
37
38
39
40
41
42
43
44
45
46
47
48
49
50
51
52
53
54
55
56
57
58
59
60
61
62
63
64
65

References

- ¹ Minh NQ. Solid oxide fuel cell technology – features and applications. *Solid State Ionics* 2004;174;271-7.
- ² Singhal SC, Kendall K. High temperature solid oxide fuel cells: fundamentals, design and applications. 1st ed. Amsterdam: Elsevier; 2003.
- ³ Singhal S. Ceramic fuel cells for stationary and mobile applications. *Am Ceram Soc Bull* 2003;82;9601-10.
- ⁴ Steele BCH, Heinzl A. Materials for fuel-cell technologies. *Nature* 2001;414;345-52.
- ⁵ Tsoga A, Naomidis A, Nikolopoulos P. Wettability and Interfacial Reactions in the Systems Ni/YSZ and Ni/Ti–TiO₂/YSZ. *Acta Mater* 1996;44;3679-92.
- ⁶ Gil V, Larrea A, Merino RI, Orera VM. Fabrication, electrochemical characterization and thermal cycling of anode supported microtubular solid oxide fuel cells. *J Power Sources* 2009;192;180-4.
- ⁷ Steele BCH. Appraisal of Ce_{1-y}Gd_yO_{2-y/2} electrolytes for IT-SOFC operation at 500 °C. *Solid State Ionics* 2000;129;95-110.
- ⁸ Markin TC, Bows RJ, Dell RM. High Temperature Solid Electrolyte Fuel Cells. Proceedings of a conference of superionic conductors. New York: Plenum Press; 1976; 15-35.
- ⁹ Minh Q. Ceramic fuel cells. *J Am Ceram Soc* 1993;3;563-88.
- ¹⁰ Finnis MW. The theory of metal ceramic interfaces. *J Phys.-Condens Mat* 1996;36;5811-36.
- ¹¹ Sinnott SB, Dickey EC. Ceramic/metal interfaces structures and their relationship to atomic- and meso- scale properties. *Matter Sci Eng R* 2003;43;1-59.
- ¹² Muñoz MC, Gallego S, Beltrán JI, Cerdá J. Adhesion at metal ZrO₂ interfaces. *Surf Sci Rep* 2006;61;303-44.
- ¹³ Orera VM, Peña JI, Merino RI, Larrea A, De la Fuente GF. Advances in science and technology. 10th International ceramics congress, CIMTEC 2002; 2003;30;885-96.

-
- 1
2
3
4
5
6
7
8
9
10
11
12
13
14
15
16
17
18
19
20
21
22
23
24
25
26
27
28
29
30
31
32
33
34
35
36
37
38
39
40
41
42
43
44
45
46
47
48
49
50
51
52
53
54
55
56
57
58
59
60
61
62
63
64
65
- ¹⁴ LLorca J, Orera VM. Directionally solidified eutectic ceramic oxides. *Prog Mat Sci.* 2006;51;711-809.
- ¹⁵ Jackson KA and Hunt JD. Lamellar and rod eutectic growth. *Trans Metal Soc AIME* 1966;1129-42.
- ¹⁶ Laguna-Bercero MA, Larrea A, Peña JI, Merino RI, Orera VM. Structured porous Ni- and Co-YSZ cermets fabricated from directionally solidified eutectic composites. *J of Eur Ceram Soc* 2005;25;1455-62.
- ¹⁷ Garcia G, Merino RI, Orera VM, Larrea A, Peña JI, Laguna-Bercero MA et al. YSZ thin films deposited on NiO-CSZ anodes by pulsed injection MOCVD for intermediate temperature SOFC applications. *Chem Vap Deposition* 2004;10;249-52.
- ¹⁸ Laguna-Bercero MA, Larrea A, Merino RI, Peña JI, Orera VM. Stability of channeled Ni-YSZ Cermets produced from self-assembled NiO-YSZ directionally solidified eutectics. *J Am Ceram Soc* 2005;88;3215-17.
- ¹⁹ Laguna-Bercero MA, Larrea A, Merino RI, Peña JI, Orera VM. Crystallography and thermal stability of textured Co-YSZ cermets from eutectic precursors. *J Am Ceram Soc* 2008;28;2325-29.
- ²⁰ Larrea A, Laguna-Bercero MA, Peña JI, Merino RI, Orera VM. Orientation relationship and interfaces in Ni and Co-YSZ cermets prepared from directionally solidified eutectics. *Cent Eur J Phys* 2009;7;242-50.
- ²¹ Ortega-San-Martín L, Peña JI, Larrea A, Orera VM. Directionally solidified CeO₂ (or GDC)/CoO eutectic ceramics as cermet precursors for SOFC anodes: microstructure cross-over. *J Eur Ceram Soc* 2011;31;1269-76.
- ²² Laguna-Bercero MA, Larrea A. YSZ-induced crystallographic reorientation of Ni particles in Ni-YSZ cermets. *J Am Ceram Soc.* 2007;90;2954-60.
- ²³ Minford WJ, Bradt RC, Stubican VS. Crystallography and microstructure of directionally solidified oxide eutectics. *J Am Ceram Soc* 1979;62;154-57.

-
- 1
2
3
4
5
6
7
8
9
10
11
12
13
14
15
16
17
18
19
20
21
22
23
24
25
26
27
28
29
30
31
32
33
34
35
36
37
38
39
40
41
42
43
44
45
46
47
48
49
50
51
52
53
54
55
56
57
58
59
60
61
62
63
64
65
- ²⁴ Wang Z, Susumu T, Saito M, Ikuhara Y. Atomic and electronic structure of the YBa₂Cu₃O₇/SrTiO₃ interface from first principles. *J Appl Phys* 2009;106;093714-1-8.
- ²⁵ Guo CX, Warschkow O, Ellis DE, Dravid VP, Dickey EC. Oxide-oxide interfaces: Atomistic and density functional study of cubic-ZrO₂(100)/NiO(111). *J Am Ceram Soc* 2001;84;2677-84.
- ²⁶ Balluffi RW, Brokman A, King AH. CSL/DSC Lattice model for general crystal-crystal boundaries and their line defects. *Acta Metall Matter* 1982;30;1453-70.
- ²⁷ Fisher CAJ, Matsubara H. Molecular dynamic simulations of interfaces between NiO and cubic ZrO₂. *Philos Mag* 2005;85;1067-88.
- ²⁸ Ikuhara Y, Pirouz P. Orientation relationship in large mismatched bicrystals and coincidence of reciprocal lattice points (CRLP). *Materials Sci Forum* 1996;207-209;121-124.
- ²⁹ Montesa CM, Shibata N, Tohei T, Ayikama K, Kuromitsu Y, Ikuhara Y. Application of coincidence of reciprocal lattice point model to metal/sapphire hetero interfaces. *Mat Sci Eng B* 2010;173;234-8.
- ³⁰ Sasaki T, Matsunaga K, Ohta H, Hosono H, Yamamoto T, Ikuhara Y. Atomic and electronic structures of Ni/YSZ(111) interface. *Mater Trans* 2004;45;2137-43.
- ³¹ Wilkinson AJ, Britton TB. Strains, planes, and EBSD in materials science. *Materials Today* 2012;15;366-76.
- ³² Gil V, Moure C, Tartaj J. *J Eur Ceram Soc* 2007;27;4205-9.
- ³³ Marlin S, Orera VM, Peña JI, Ortega-San-Martín L, Molten cermet material, Patent application publication WO 2010/103498 A1.
- ³⁴ Ortega-San-Martín L, Peña JI, Larrea A, Gil V, Orera VM. Textured cermets of CeO₂ (or GDC) with Co for solid oxide fuel cells anodes. *Int J Hydrogen Energ* 2010;35;11499-504.
- ³⁵ Chen M, Hallstedt B, Grundy AN, Gauckler LJ. CeO₂-CoO phase diagram. *J Am Ceram Soc* 2003;86;1567-70.
- ³⁶ Channel 5. Oxford Instruments HKL. ® HKL Technology 2006. Denmark.
- ³⁷ Ashcroft NW, Mermin ND. *Solid state physics*. 1st ed. Saunders College Publishing; 1976.

-
- 1
2
3
4
5
6
7
8
9
10
11
12
13
14
15
16
17
18
19
20
21
22
23
24
25
26
27
28
29
30
31
32
33
34
35
36
37
38
39
40
41
42
43
44
45
46
47
48
49
50
51
52
53
54
55
56
57
58
59
60
61
62
63
64
65
- ³⁸ Bunge HJ. Texture analysis in materials science: mathematical methods. 2nd ed. London: Butterworths; 1982.
- ³⁹ Revcolevschi A, Dhalenne G, d'Yvoire F. Growth of nickel-oxide-based oriented eutectic structures and characterization of the interphase boundaries. *J Phys-Paris*. 1985;46;441-7.
- ⁴⁰ Dickey EC, Dravid VP, Nellist PD, Wallis DJ, Pennycook SJ. Three-dimensional atomic structure of NiO-ZrO₂ (cubic) interfaces. *Acta Mater* 1998;46;1801-16.
- ⁴¹ Bonvalot-Dubois B, Dhalenne G, Revcolevschi A. Electrochemical-behavior of lamellar interfaces in CoO-ZrO₂(CaO) aligned eutectic structures submitted to chemical-reduction. *Mater Res Soc Symp Proc* 1989;138;587-92.
- ⁴² Echigoya J, Hayashi S, Aoyagi E. Interface structure of Co-ZrO₂ eutectics. *J Cryst Growth* 1993;129;699-705.
- ⁴³ Dickey EC, Fan X, S.J. Pennycook. Direct atomic-scale imaging of ceramic interfaces. *Acta Mater*. 1999;47;4061-68.
- ⁴⁴ Barin I. Thermochemical data of pure substances. 3rd ed. Weinheim: VCH Verlagsgesellschaft; 1995.
- ⁴⁵ Hunt JD, Jackson KA. Binary eutectic solidification. *Trans. AIME* 1966;236;843.
- ⁴⁶ Kurz W, Fisher DJ. Fundamentals of Solidification. 4th ed. Switzerland: Trans Tech Publications Ltd.; 1992.
- ⁴⁷ Larrea A, Orera VM, Pena JI, Merino RI. Orientation relationships and interfaces in nonfaceted-nonfaceted ZrO₂(c)-CaZrO₃ lamellar eutectics. *J Mater Res* 1999;14;2588-93.
- ⁴⁸ Xing JJ, Takeguchi M, Tanaka M, Nakayama Y. Reduction of a NiO thin film deposited by PLD on a single crystal YSZ (111) substrate. *J Mater Sci* 2012;47;5254-62.
- ⁴⁹ Pauling L. The principles determining the structure of complex ionic crystals. *J Am Chem Soc* 1929;51;1010-26.
- ⁵⁰ Tiller WA. Liquid metals and solidification. American Society for Metals, Metals Park, Ohio: ASM; 1958; 279-318.

⁵¹ Frank FC, Vandermerwe JH. One-dimensional dislocations. 2. Misfitting monolayers and oriented overgrowth. P Roy Soc Lond A Mat 1949;198;216-225.

1
2
3
4
5
6
7
8
9
10
11
12
13
14
15
16
17
18
19
20
21
22
23
24
25
26
27
28
29
30
31
32
33
34
35
36
37
38
39
40
41
42
43
44
45
46
47
48
49
50
51
52
53
54
55
56
57
58
59
60
61
62
63
64
65

FIGURE CAPTIONS

Fig. 1. Kikuchi pattern acquired on a YSZ lamella of a CoO-YSZ specimen, (a) as acquired and (b) after indexation of the bands to determine the crystallographic orientation (round markers signal the main YSZ zone axes). The acceleration voltage was 20 kV and the probe current, 0.8 nA.

Fig. 2. EBSD orientation map of a CoO-YSZ sample solidified at 100 mm/h. Pixels with the same grey level correspond to surface areas with the same orientation. Within each eutectic grain, each phase behaves as a single crystal.

Fig. 3. Experimental pole figures for two different areas of the same transverse cross-section of a NiO-YSZ sample. In 3(a) the pole figures show growth direction GD1: $\langle 110 \rangle$ for NiO and $\langle 100 \rangle$ for YSZ (b). In 3(b) the pole figures show growth direction GD2: $\langle 110 \rangle$ for NiO and $\langle 110 \rangle$ for YSZ. In both cases, the interface plane is $\{001\}_{\text{YSZ}} // \{111\}_{\text{NiO}}$, highlighted by a square marker, while growth directions are signaled by round markers.

Fig. 4. (a) Forescatter image of a longitudinal cross-section of NiO-YSZ solidified at 10 mm/h. Surface relief due to differential polishing produces the contrast. (b) Orientation map of the same area. The absence of contrast indicates the presence of the cube-on-cube orientation relationship, where the two phases are parallel.

Fig. 5. (a) Orientation map of a CoO-GDC fibrillar area. The phases display a well-defined OR, the same as in the lamellar areas. (b) Orientation map of a CoO-YSZ fibrillar area. The different grey levels indicate different orientations of the fibres.

Fig. 6. Coincidence of atoms at the $(001)_{\text{YSZ}}// (111)_{\text{NiO}}$ interface plane. Filled-in circles stand for $(001)_{\text{YSZ}}$ oxygen anions while unfilled-in circles represent $(111)_{\text{NiO}}$ nickel cations. Growth directions GD1 and GD2 are indicated in the figure.

Fig. 7. (a) High overlapping zones of the 3D Euler space, according to the CRLP model applied to NiO-YSZ. (b) Normalized overlapped volume as a function of the α and β Euler angles ($\gamma=0^\circ$).

TABLE CAPTIONS

Table 1: Composition, solidification rates and interphase spacing of the studied DSE.

Table 2: Growth directions (GD1 or GD2, see main text) found for each material and solidification rate.

Table 3: Ionic charge density for some low-Miller-indices polar planes, calculated for the indicated cell parameter, a .

Table 4: Misfit between the ionic charge density of the $(111)_{\text{TMO}}// (001)_{\text{IC}}$ polar planes calculated for each material.

Table 5: Misfit between lattice parameters along the close-packed directions of the interface planes, $[\bar{0}11]_{\text{TMO}}// [010]_{\text{IC}}$, and along the crystallographic directions perpendicular to the close-packed ones, $[\bar{2}\bar{1}\bar{1}]_{\text{TMO}}// [100]_{\text{IC}}$, for each DSE.

Table 1

| Eutectic material | Composition (mol%) | Solidification rate (mm/h) | Interphase spacing λ (μm) |
|------------------------|---------------------------------|----------------------------|--|
| NiO – YSZ | 77 % NiO, 23 % YSZ | 10, 50, 100 | 0.2 - 3 |
| CoO – YSZ | 80 % CoO, 20 % YSZ | 10, 50, 100 | 0.5 - 3.4 |
| NiO – GDC | 73 % NiO, 27 % GDC | 10, 50, 100 | 0.7 - 3.8 |
| NiO – CeO ₂ | 73 % NiO, 27 % CeO ₂ | 10, 50, 100 | 0.5 - 3 |
| CoO – GDC | 82 % CoO, 18 % GDC | 10, 50, 100, 200 | 0.7 - 3.8 |
| CoO – CeO ₂ | 82 % CoO, 18 % CeO ₂ | 10, 50, 100, 200 | 0.5 - 3.4 |

Table 1: Composition, solidification rates and interphase spacing of the studied DSE.

Table 2

| Solidification rate | NiO-YSZ | CoO-YSZ | NiO-GDC | NiO-CeO ₂ | CoO-GDC | CoO-CeO ₂ |
|---------------------|------------|---------|---------|----------------------|---------|----------------------|
| 10 mm/h | GD1 GD2 | GD1 | GD1 | GD2 | GD1 | GD2 |
| 50 mm/h | GD1 GD2 | GD1 | GD1 | GD2 | GD1 | GD1 GD2 |
| 100 mm/h | GD2 | GD1 | GD1 | GD2 | GD2 | GD1 |
| 200 mm/h | - | - | - | - | GD1 | GD2 |

Table 2: Growth directions (GD1 or GD2, see main text) found for each material and solidification rate.

Table 3

| | Ionic charge density ($e^-/\text{\AA}^2$) | | | | Ionic charge density ($e^-/\text{\AA}^2$) | |
|----------------------|---|-------|------------------|-------|---|-------|
| | YSZ | GDC | CeO ₂ | | NiO | CoO |
| a (\AA) | 5.127 | 5.418 | 5.411 | | 4.179 | 4.252 |
| {111} | 0.338 | 0.307 | 0.315 | {111} | 0.265 | 0.255 |
| {100} | 0.292 | 0.266 | 0.273 | {311} | 0.138 | 0.133 |
| {311} | 0.177 | 0.160 | 0.165 | {331} | 0.105 | 0.101 |
| {331} | 0.134 | 0.122 | 0.125 | {511} | 0.088 | 0.085 |
| {102} | 0.130 | 0.119 | 0.122 | {531} | 0.077 | 0.075 |
| {221} | 0.098 | 0.089 | 0.091 | {551} | 0.064 | 0.062 |
| {308} | 0.034 | 0.031 | 0.032 | {771} | 0.046 | 0.044 |

Table 3: Ionic charge density for some low-Miller-indices polar planes, calculated for the indicated cell parameters, a .

Table 4

| | NiO-YSZ | CoO-YSZ | NiO-GDC | NiO-CeO ₂ | CoO-GDC | CoO-CeO ₂ |
|------------|---------|---------|---------|----------------------|---------|----------------------|
| Misfit (%) | 9.9 | 13.6 | 0.5 | 2.9 | 4.3 | 6.7 |

Table 4: Misfit between the ionic charge density of the (111)_{TMO}//(001)_{IC} polar planes calculated for each material.

Table 5

| | Misfit along the close-packed directions | Misfit along the perpendicular to the close-packed directions |
|------------------------|--|---|
| NiO - YSZ | 14 % | 0 % |
| CoO - YSZ | 16 % | 2 % |
| NiO - GDC | 8 % | 6 % |
| NiO - CeO ₂ | 8 % | 6 % |
| CoO - GDC | 10 % | 4 % |
| CoO - CeO ₂ | 10 % | 4 % |

Table 5: Misfit between lattice parameters along the close-packed directions of the interface planes, $[0\bar{1}1]_{\text{TMO}}/[010]_{\text{IC}}$, and along the crystallographic directions perpendicular to the close-packed ones, $[\bar{2}1\bar{1}]_{\text{TMO}}/[\bar{1}00]_{\text{IC}}$, for each DSE.

Figure 1a
[Click here to download high resolution image](#)

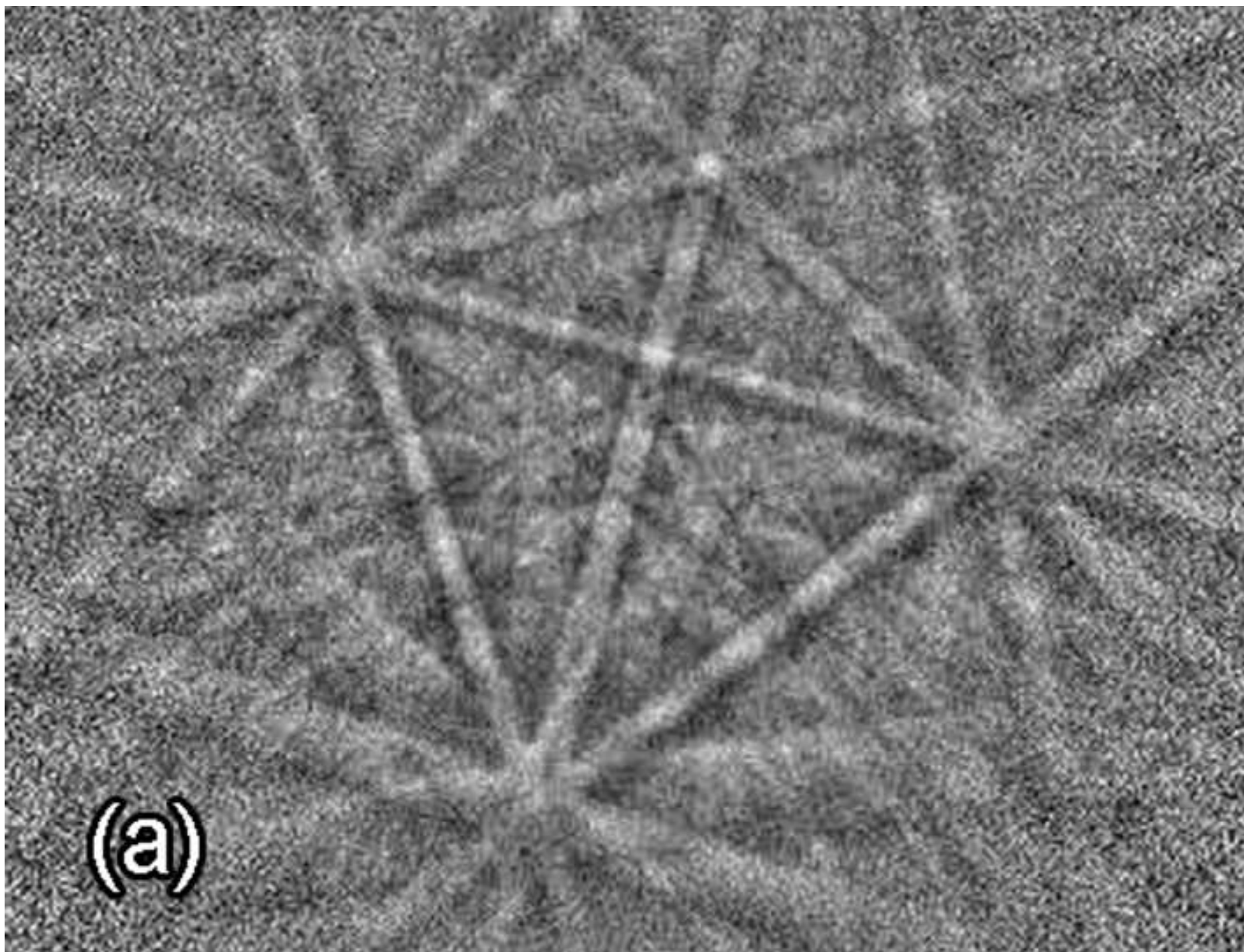


Figure 1b
[Click here to download high resolution image](#)

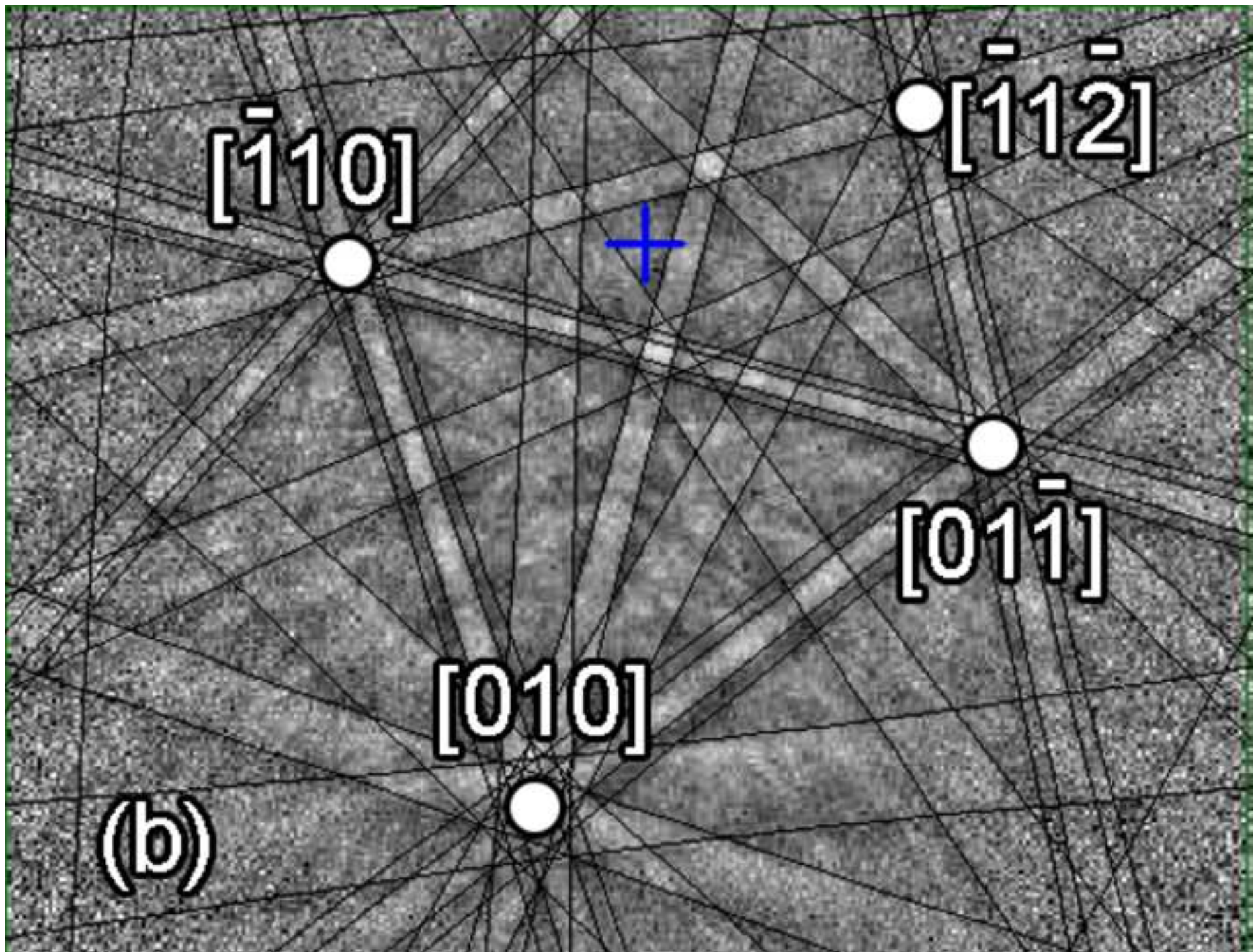


Figure 2
[Click here to download high resolution image](#)

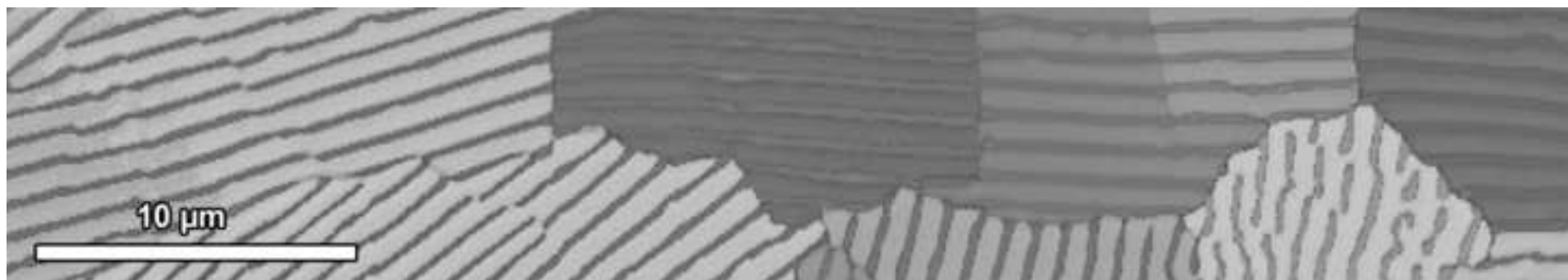


Figure 3a
[Click here to download high resolution image](#)

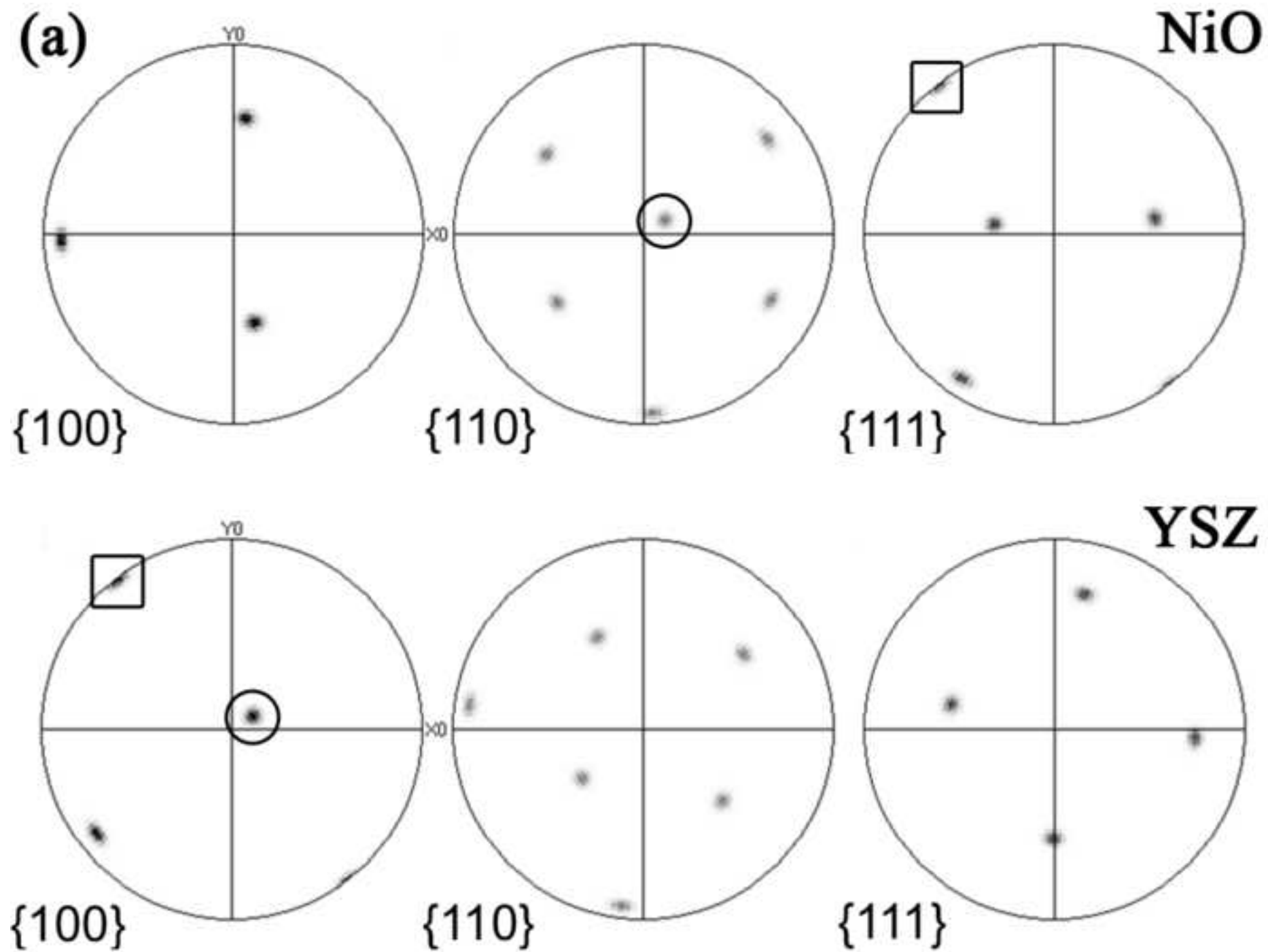


Figure 3b
[Click here to download high resolution image](#)

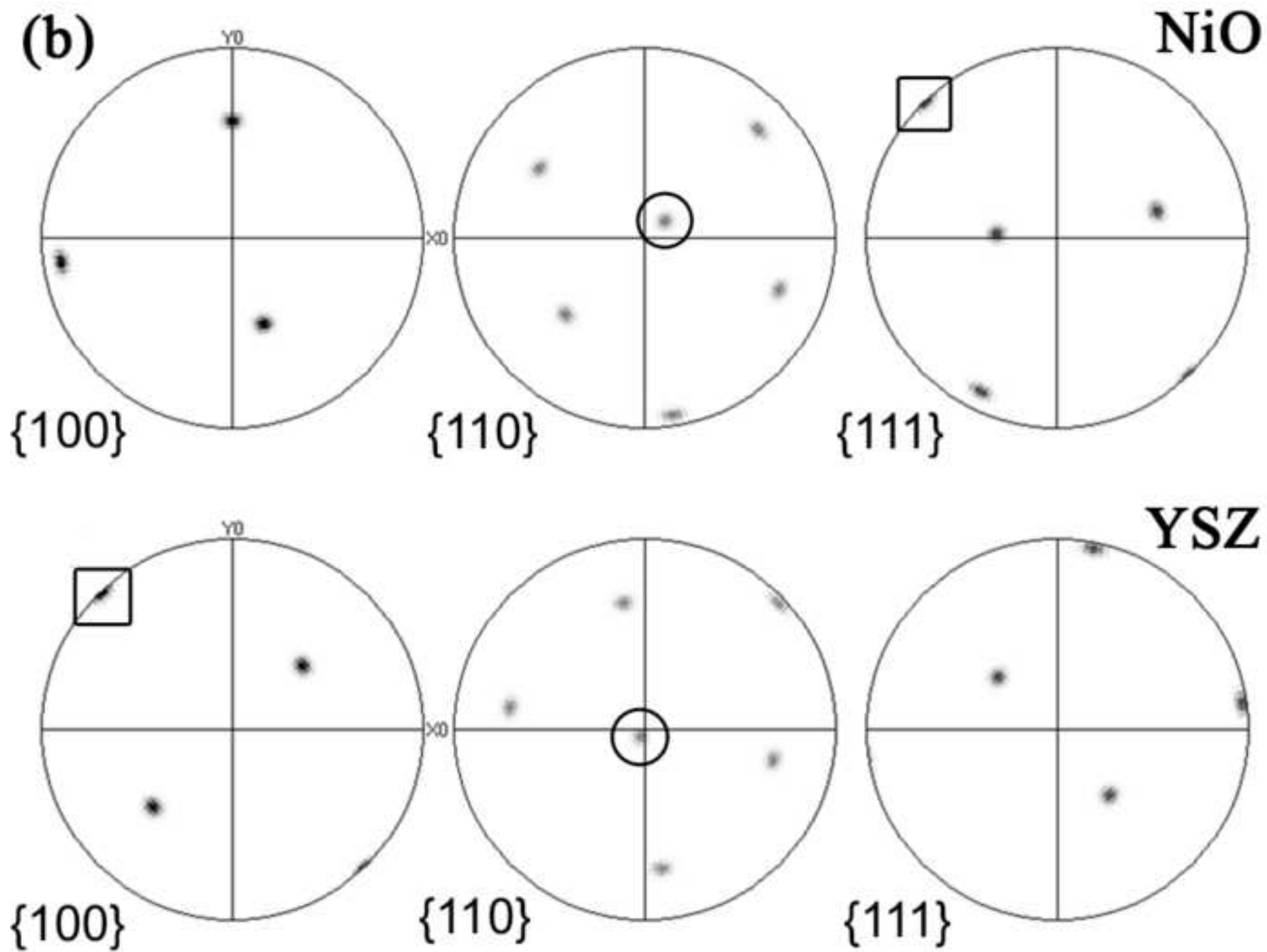


Figure 4a
[Click here to download high resolution image](#)

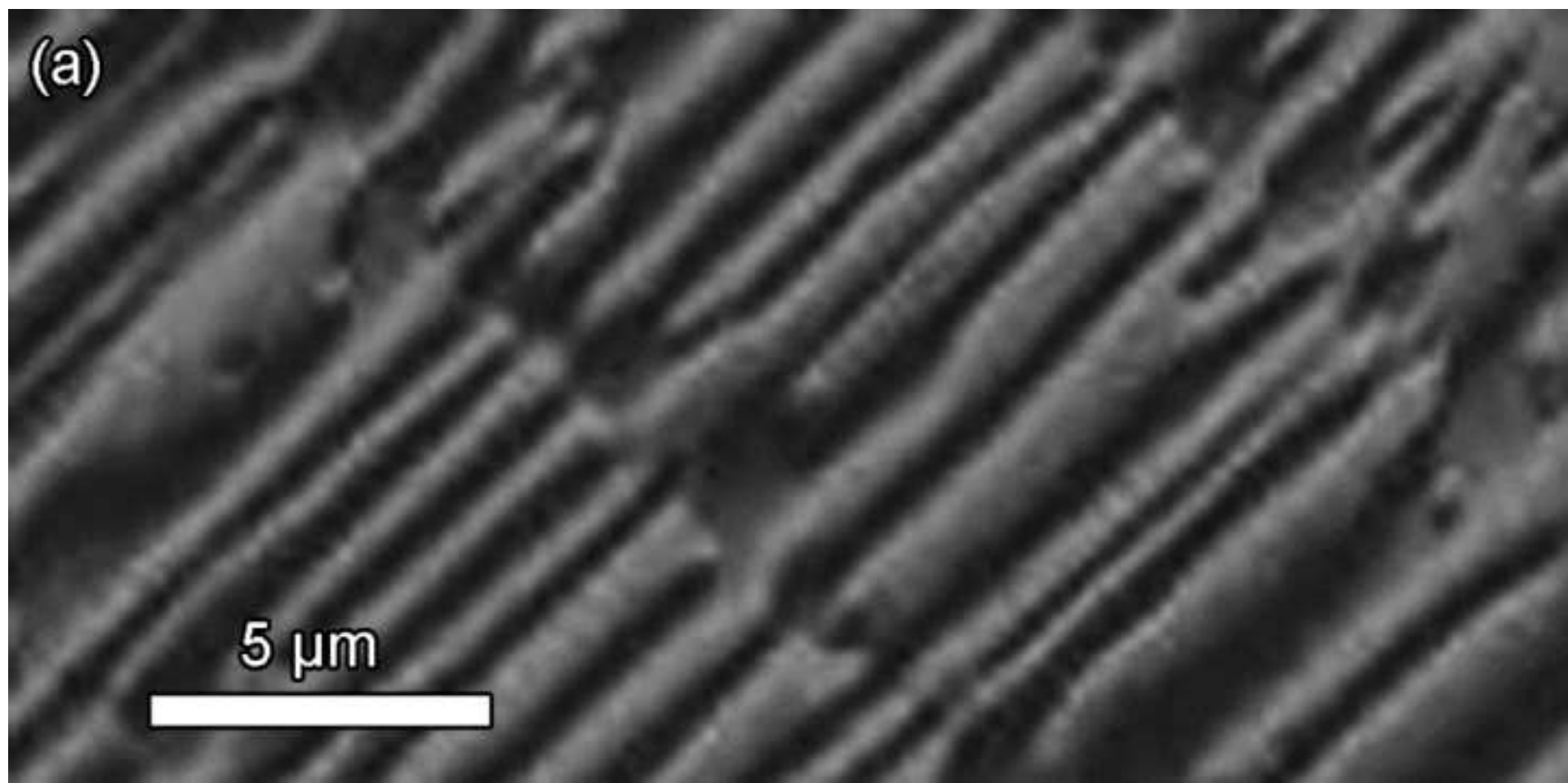


Figure 4b
[Click here to download high resolution image](#)

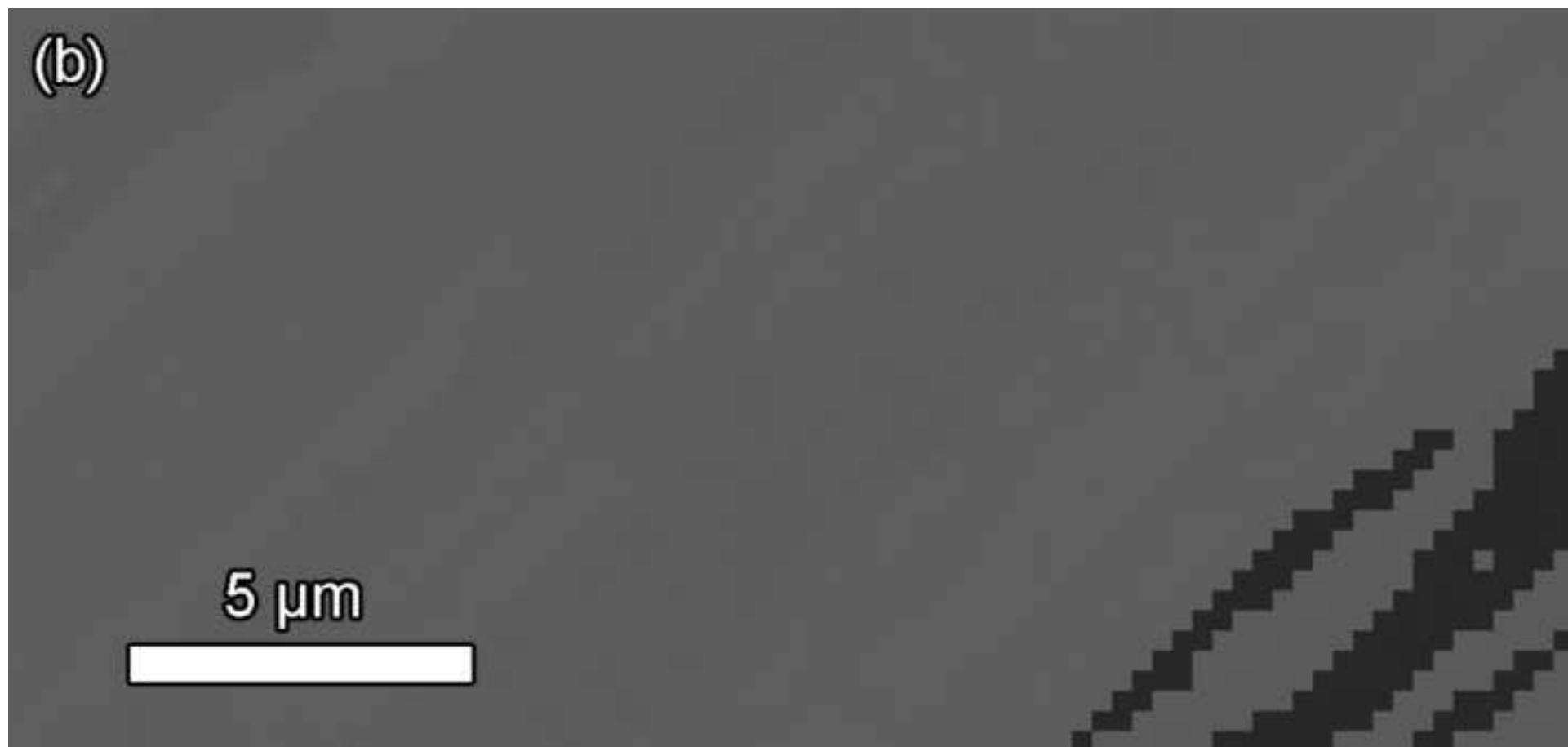


Figure 5a
[Click here to download high resolution image](#)

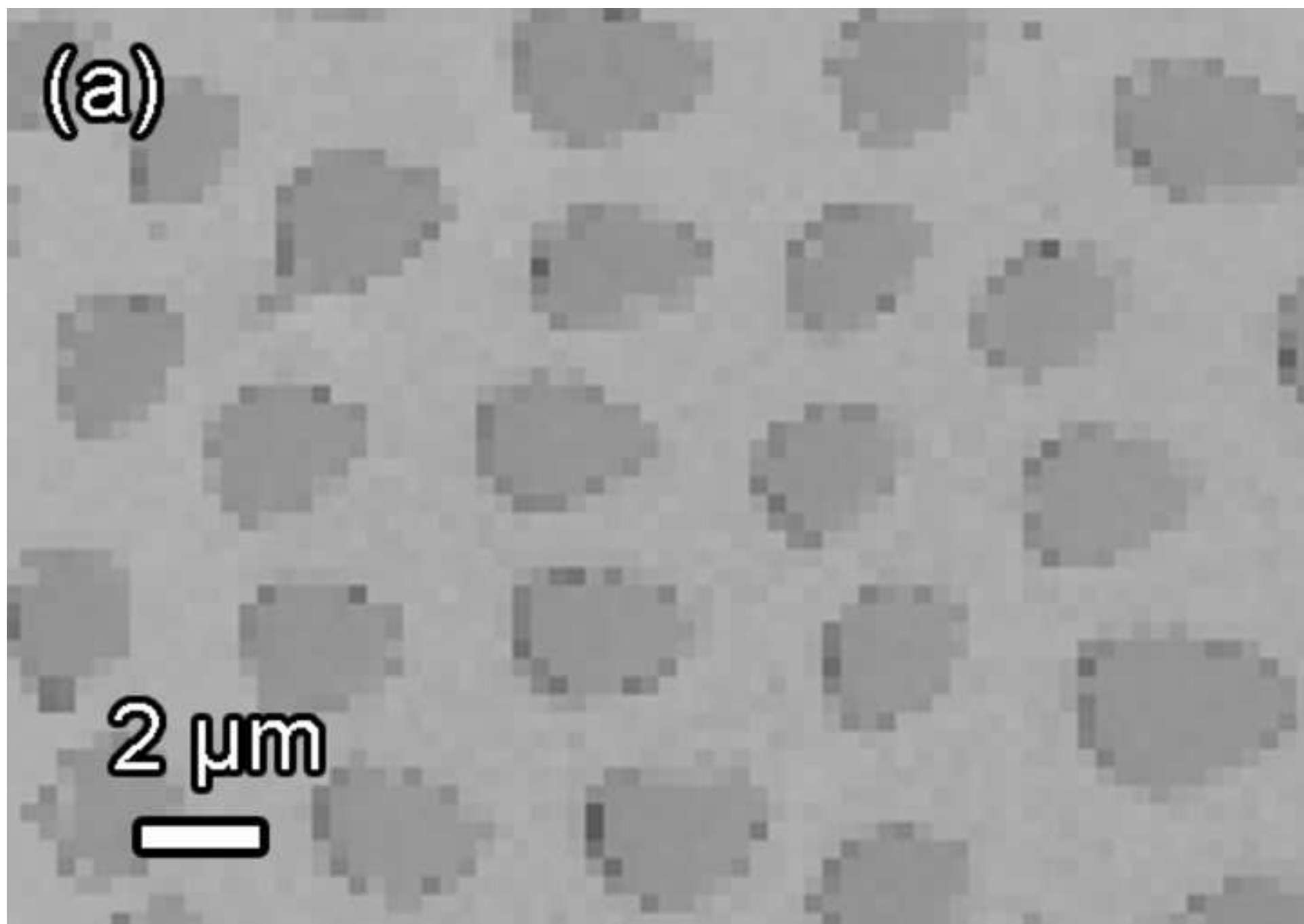


Figure 5b
[Click here to download high resolution image](#)



Figure 6
[Click here to download high resolution image](#)

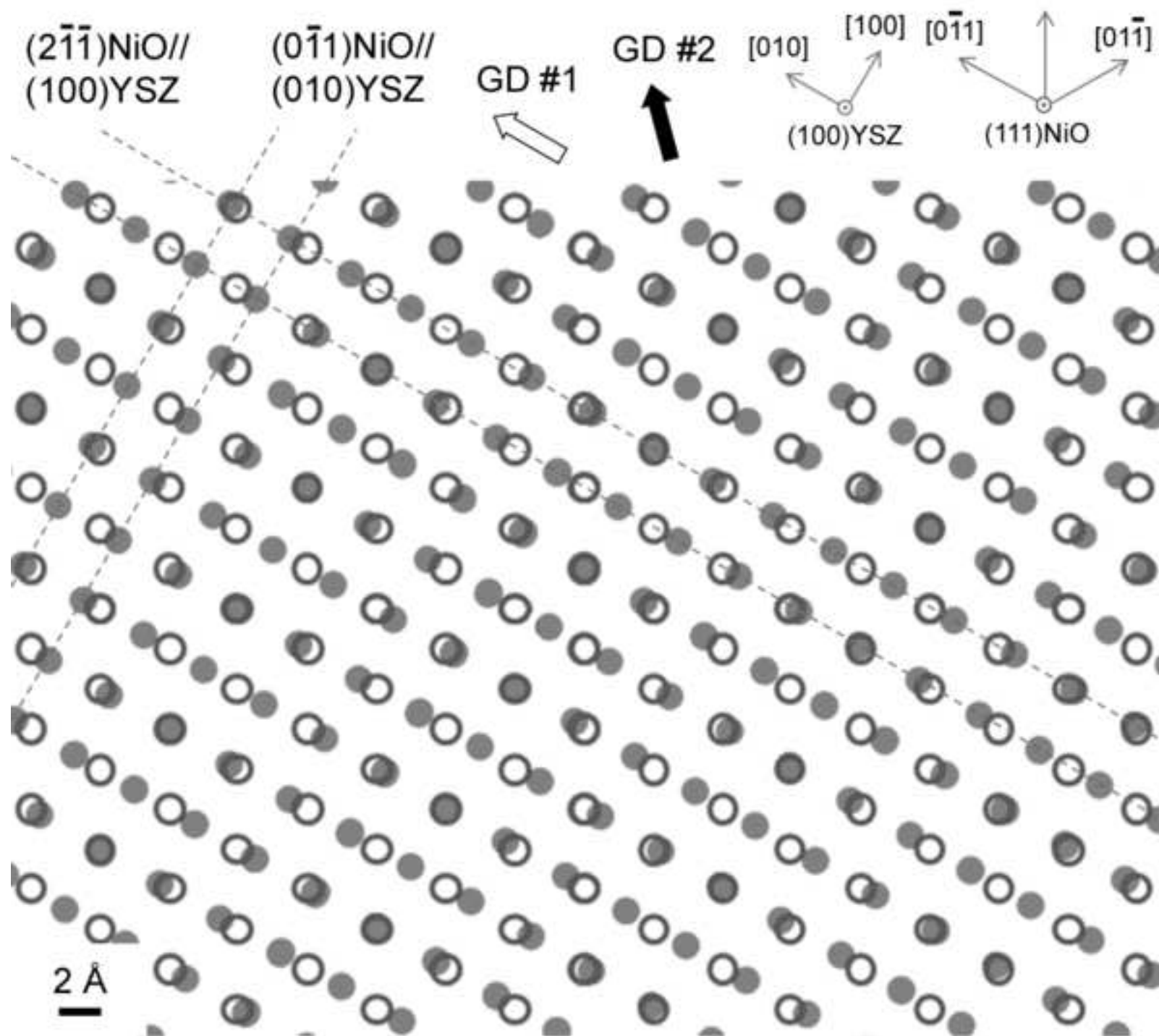


Figure 7a
[Click here to download high resolution image](#)

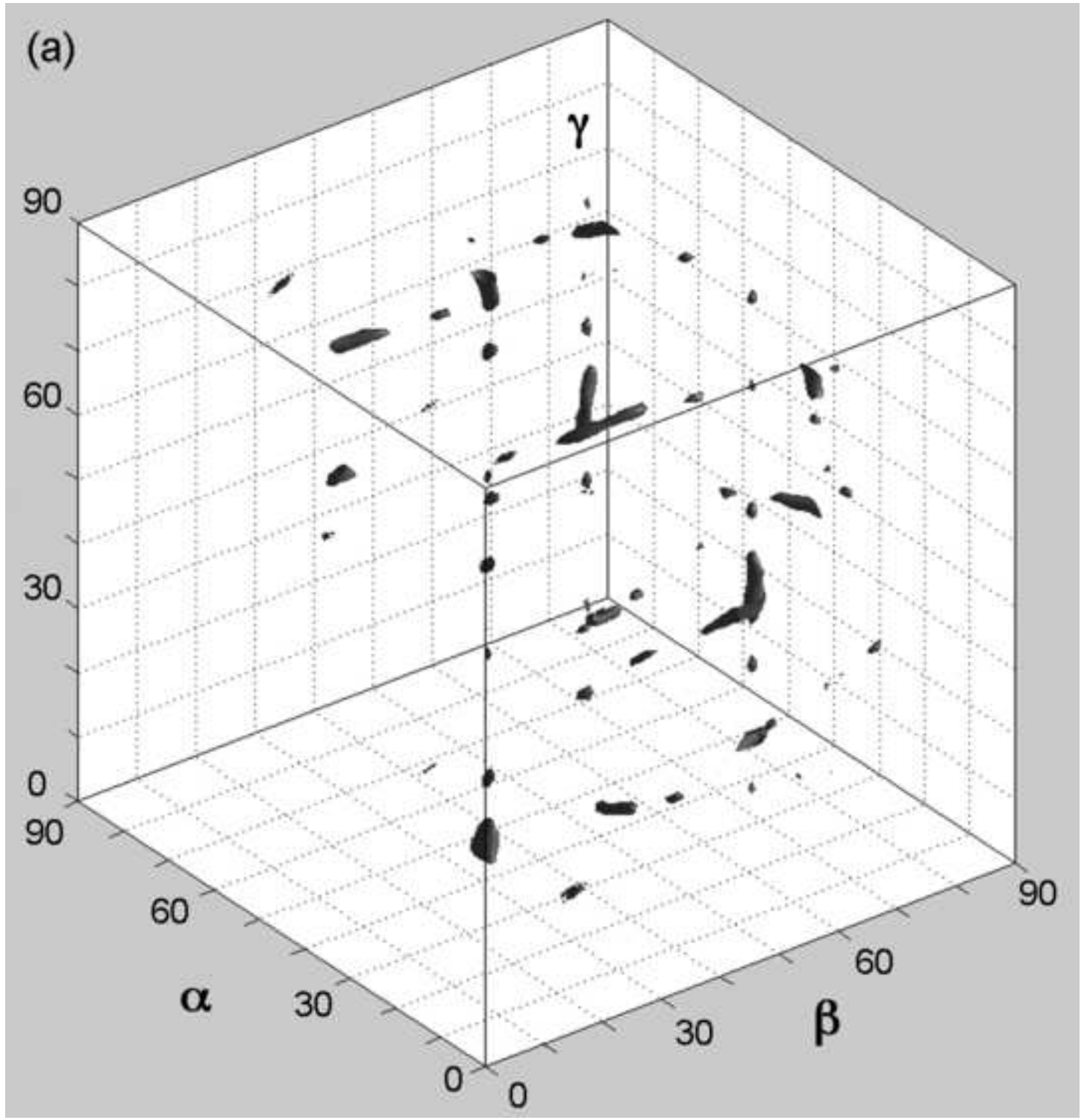


Figure 7b
[Click here to download high resolution image](#)

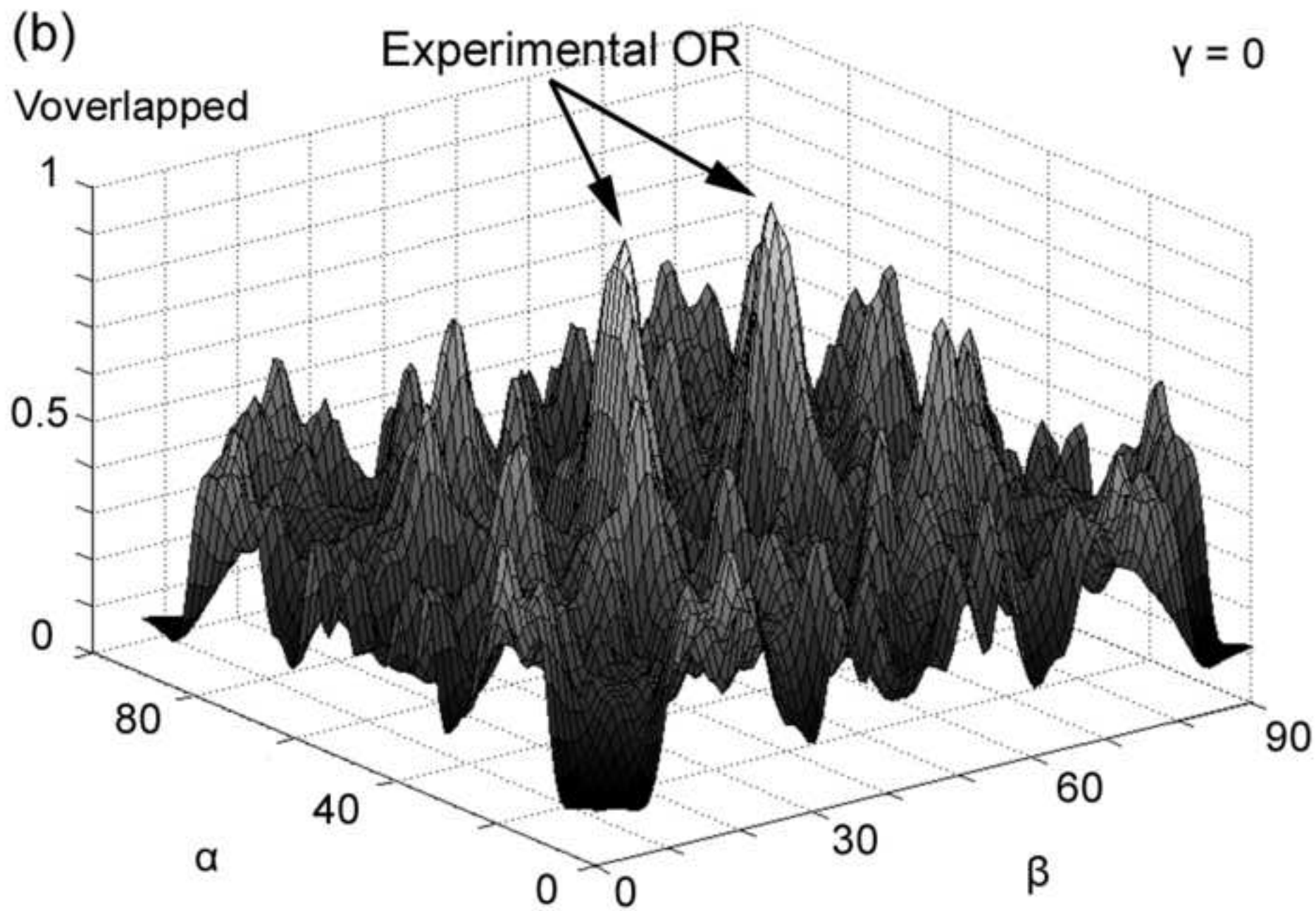


Figure 2 color

[Click here to download Electronic Annex: Fig2color.tif](#)

Figure 4b color

[Click here to download Electronic Annex: Fig4bcolor.tif](#)

Figure 6 color

[Click here to download Electronic Annex: Fig6color.tif](#)

Figure 7a color

[Click here to download Electronic Annex: Fig7acolor.tif](#)